Synthetic helium beam diagnostic and underlying atomic data

W Zholobenko[1,2], M Rack[1,3], D Reiter[1], M Goto[4], Y Feng[2], B Küppers[1] and P Börner[1]

[1] Forschungszentrum Jülich GmbH, Institut für Energie- und Klimaforschung – Plasmaphysik, Partner of the Trilateral Cluster (TEC), 52425 Jülich, Germany
[2] Max-Planck-Institut für Plasmaphysik, 85748 Garching / 17491 Greifswald, Germany
[3] JARA-HPC, Forschungszentrum Jülich GmbH, 52425 Jülich, Germany
[4] National Institute for Fusion Science, Toki 509-5292, Japan

E-mail: wlz@ipp.mpg.de

Abstract. We report on synthetic helium beam emission spectroscopy (BES) in fusion edge plasmas, as enabled by the 3D kinetic (neutral particle) transport code EIRENE. We also review and upgrade the underlying atomic helium data base, resorting to the most recent version of the Goto-Fujimoto collisional-radiative code and a recommended and publicly exposed reference cross section data set from an internationally coordinated (IAEA) evaluation activity. On the example of the Wendelstein 7-X (W7-X) stellarator, we use both the upgraded transport code and data base to simulate the penetration of and radiation from thermal helium used for BES in the island divertor region. This allows to evaluate the applicability of the diagnostic in different plasma backgrounds, simulated with the 3D edge plasma Monte Carlo code EMC3-EIRENE, and with different levels of refinement of underlying atomic data. The sensitivity of the diagnostic to the atomic data set – which is crucial for a quantitative determination of electron density and temperature profiles – is investigated and discussed, as well as the effects of p-He beam widening and correlated line-of-sight integration.

Keywords: synthetic diagnostic, He beam, collisional-radiative model, EIRENE code, Wendelstein 7-X, correlated line-of-sight integration
Submitted to: *Nucl. Fusion*

1. Introduction

The He-beam spectroscopy in hydrogen fusion plasmas has become a standard edge plasma diagnostic in magnetic fusion research. It was originally developed [1] and applied [2, 3] at the TEXTOR tokamak for the measurement of electron temperature T_e and density n_e in the plasma boundary.

Since then active beam emission spectroscopy (BES) using helium gas injection is being applied at many fusion experiments, e.g. at the JET [4] and ASDEX Upgrade [5] tokamaks, or at the W7-X [6] and TJ-II [7] stellarators. Passive helium spectroscopy (without beam injection) is also applied frequently, e.g. at the TJ-II [7] and LHD [8] stellarators and at the linear divertor simulator NAGDIS-II [9]. Passive helium spectroscopy is especially interesting in burning reactor plasmas since these will unavoidably have to contain significant concentrations of helium in the divertor [10].

Despite its widely spread applications since more than two decades now, this plasma diagnostic still poses a number of challenges, e.g. finite meta-stable relaxation times [8, 11], heavy particle collisions between helium and hydrogenic plasma constituents, especially non-symmetric charge exchange (CX) [12, 5].

A persistent difficulty is to acquire reliable and publicly exposed atomic collision data: they are needed to obtain reaction rates in the "collisional-radiative (CR) models", a set of coupled rate equations for the populations of electronically excited helium states. Their solution, together with radiative transition rates, provides the atoms' light emissivity, which depends on local plasma parameters electron temperature T_e and density n_e. In this work, we use the well established helium CR model by Goto [13] (referred to as GCRM here): it contains an internationally evaluated data set of electron impact excitation and ionization cross sections, compiled by Ralchenko *et al.* [14], and spontaneous decay and singlet-triplet wave function mixing data given in [15].

Helium BES application in detached stellarator plasmas is further challenged by complex geometries and spatial plasma inhomogeneities, high electron densities ($n_e \gtrsim 10^{14}$ cm^{-3}) and low electron temperatures ($T_e \lesssim 20$ eV). The latter plasma parameters lie in a still rather unexplored parameter range of the helium beam diagnostic [16] and may require to account for additional effects such as recombining plasma conditions with a mix of three-body, radiative and di-electronic recombination into the light emitting electronically excited states of He atoms [9]. Also finite opacity [8, 9, 17, 18] as well as stronger frictional hydrogen-helium transport effects may set in.

Appropriate atomic data for the mentioned recombination processes are already included in GCRM (loc. cit.).

In this present work we mainly focus on upcoming challenges for the divertor campaign at W7-X because it requires the consideration of all of the above mentioned effects. The particular hardware set up is described in [19, see also figure 1], including the gas injection and observation system. However, the computational tools and the atomic cross section reference data base exposed here may be useful for helium spectroscopy in magnetic fusion devices in general. For instance, we discuss the implication of the singlet-triplet state mixing [13], which concerns the applicability of helium emission spectroscopy at higher magnetic fields, such as in ITER.

Our computational approach here to address these numerous challenges is a fully three dimensionally resolved "synthetic He beam diagnostic", utilizing the 3D particle

transport options and further extended post processing features in the (neutral particle) 3D transport code EIRENE [20, 21].

By contrast to the interpretative application of helium CR models directly (or with strong simplifying transport assumptions as in [11]) to experimentally observed helium light emission, the internal consistency of the helium BES and its interpretation can be evaluated on a far better controlled (albeit simulated) 3D plasma state from a forward transport calculation of main plasma plus helium beam, both with the same atomic data base. Many details affecting the precision of the BES diagnostic method can be taken into account one by one, such as 3D transport, non-equilibrated meta-stable states, thermal spread in the helium beam, or opacity.

Supplementary material and technical details, also on recent code extensions and new options in the "EIRENE diagnostic module" (section 2), are given in [22].

This paper is organised as follows. In section 2, a review is given on the EIRENE diagnostic module, its features and past applications, with focus on differences and similarities between H and He spectroscopy. We then describe our current application to W7-X in section 3. In section 4, the model of the diagnostic module and its application to BES is elucidated, and its usefulness to experimental application is specified. The CR model GCRM is described in section 5. The cut-off in a CR model, the highest bound atomic level, is still often chosen very differently [23, 12, 13, 11]. We therefore revisit this issue in section 6. The singlet-triplet state mixing generally leads to an explicit B-field dependence in a CR model, potentially being a challenge for e.g. ITER diagnostics. However in section 7 we argue that for medium sized fusion experiments like W7-X, with $B \in [0.2, 3.7]$ T, a constant data correction is sufficient. Additional widening of the beam due to elastic proton collisions is quantified in section 8. In section 9 the diagnostic evaluation algorithm is explained and applied to the investigation of the finite meta-stable equilibration time effect. Finally, we quantify the effect of correlated line-of-sight integration on measured T_e and n_e in section 10. Conclusions are then summarised in section 11.

2. The EIRENE code diagnostic module

The EIRENE "synthetic diagnostic module" [20, section 2.12] is part of the standard post processing options provided together with the transport code itself, and is distributed widely since a few decades now. It is routinely used e.g. to analyse the reconstruction of the hydrogen recycling flux from camera images of visible hydrogen light emission, most often done so by comparison with synthetic line-of-sight integrated Balmer line emission intensities. In particular for hydrogenic emission it is well known that this poses a rather complex inverse problem because several significant emission channels of quite different physical origins overlap, for any given hydrogenic line. We will argue below that very similar issues exist for He BES, which led to a generalization of the diagnostic module in EIRENE.

For hydrogen, there are direct contributions, originating from electron and resonant proton impact processes (and subsequent spontaneous line emission) on the H, H_2, H_2^+, H_3^+, H^- and H^+ donor states. Since the EIRENE code provides the solution to the 3D transport problem also with full resolution in velocity space, these contributions have sometimes been identified by their distinctly

Doppler broadened line shapes − see [24] for an early 2D experimental validation application using TEXTOR limiter discharges. To compare this synthetic *line shape* option of EIRENE to experimental data requires high resolution spectroscopy. Therefore mostly only the (integrated over emission line profile) *line intensities* have been used, the latter then line-of-sight integrated for each synthetic camera pixel.

For a 3D spatially resolved stellarator configuration (TJ-II) such synthetic diagnostics applications of EIRENE have been reported in [25]. As confirmed there, the consideration of several relevant emission channels, in particular those from dissociation of ionized H_2 molecules, can be important. A recent application of this tool particularly for W7-X conditions, again for side-on integrated line intensities of hydrogen line emission, is carried out in [26, 27], and again with similar conclusions.

Notably, for helium BES similar inversion issues exist, although for other physical reasons: the emission in any particular neutral helium atom line is, in principle, also simultaneously coupled to various donor states − to the helium ground, the meta-stable and the helium ion donor states. In fusion edge plasmas these donor states may not be collisional-radiative equilibrated amongst themselves at the location of light emission, but their concentrations follow from a "transport equilibrium" instead.

In helium BES the recombining component (coupling to the He^+ ion) can usually be neglected. But distinct from the hydrogen case the three remaining components, the helium ground and two meta-stable states, are not significantly separated in velocity space, so that the Doppler line shape resolved high resolution spectroscopy option does not provide sufficient additional information. Therefore, until now, only line intensities (rather than emission line shapes) seem to have been considered, both experimentally and numerically. This will also remain to be the case in the present work.

The inversion problem is further complicated by the line-of-sight integration in space, as discussed in [26, 27] for hydrogen. We revisit the non-local effects on side-on-integration in section 4, arguing that they are even more severe for the (commonly used in He BES) line intensity ratios. In section 10, we quantify the effect on our current simulations for W7-X, after separating it from the impact of meta-stable state transport in section 9.

In order to fully capture these transport effects, in the present work the (local) helium CR code [13] was coupled to both the forward transport simulation of the thermal beam and to the inverse plasma reconstruction from line-of-sight integrated synthetic camera pictures. Details on the extended implementation and options are given in the EIRENE online manual [20, section 2.12].

An important feature of the EIRENE code is the very flexible choice of atomic and molecular interactions for any given transport problem by selecting from various properly formatted external databases or internal (linear) collisional-radiative codes. The database has now been supplemented with an updated CR model [13], replacing its earlier (also already meta-stable resolved) He database [28], see section 5 below.

The transport-reaction simulations carried out in the present work account for all electron impact collision processes and radiative decay in [13] and, additionally, elastic proton-helium heavy particle reactions [29] from the EIRENE data base [20, A&M Data, Amjuel]. Further reaction channels, e.g. non-symmetric charge exchange or data for the formation of exotic molecules such as the hydro-

helium cation, could be included in the simulation, should experimental evidence require so.

In past versions EIRENE further did contain an integrated radiation transport module: if re-activated this would allow to take account of radiation trapping effects [30, 31]. Radiation trapping for hydrogen was observed e.g. at the Alcator C-Mod [32] and JET [33] tokamaks. For helium, there are indications from the LHD stellarator [8]. In linear devices like NAGDIS-II [9] and PISCES-A [17] radiation trapping is pronounced due to high neutral gas densities, requiring the calculation of radiation transport [18]. In fact, we estimate the optical thickness to be significant already for our current simulations [22, chapter 8.3.2]. Therefore, re-activation of the module is in progress.

3. Application to W7-X

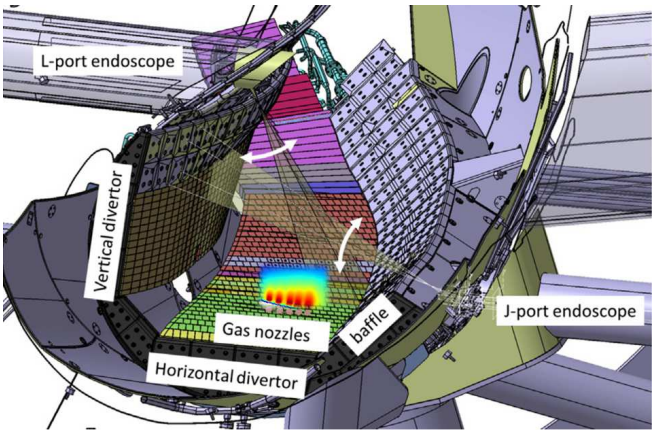

Figure 1: Gas inlets and observation geometry for spectroscopy in a lower W7-X divertor, amended from [19], plus simulated helium gas distribution (figure 2 mirrored vertically). The set-up in the upper divertor is equivalent up to vertical mirroring. The endoscope mirrors and hence the view cones are moveable, allowing to capture the emission from both ports.

We use these features to analyse the emission from thermal atomic He beams installed at the divertor of W7-X [19]. Parameters of the gas injection system were extracted from [6, 34]. The set-up for the lower divertor is shown in figure 1. An identical set-up, connected to the one in the lower divertor by an island chain, is installed in the upper divertor. Here, we will focus on the upper divertor, following the experimental work by [6]. Using both endoscope cameras, it is foreseen to reconstruct the spatial emission distributions of the five beams by tomographic methods. Without tomography, however, the emission of different beams overlaps for the camera views available in the experiment.

By contrast, synthetic spectroscopy provides the complete 3D emission profile and a virtual camera can, in principle, be located anywhere. Therefore, we can circumvent tomography by directly evaluating the poloidal emission profile. This will be done quantitatively in section 9. Here, we show in figure 2 for illustrative purposes a synthetic camera picture of the poloidal plane at the location of the five gas nozzles, viewed by a virtual camera placed 1 m (toroidally) away from this plane. To elucidate the set-up, we also use it mirrored vertically as inset in figure 1.

It is intended to measure T_e and n_e in a broader spatial region in the experiment by using five beams and tomographic reconstruction. They are shown here to demonstrate this hardware set-up. However, for clarity of the evaluation of the diagnostic, we will focus on only the middle one of the five beams in following sections.

The He beams and their emission were calculated by EIRENE on a pure hydrogen plasma state, consisting of 3D profiles of T_i, T_e, $n_\mathrm{e} = n_\mathrm{i}$, and the parallel plasma flow $V_\parallel$, generated by the EMC3-EIRENE code package [35]. The T_e and n_e profiles, necessary for our analysis, are displayed in figure 3 for

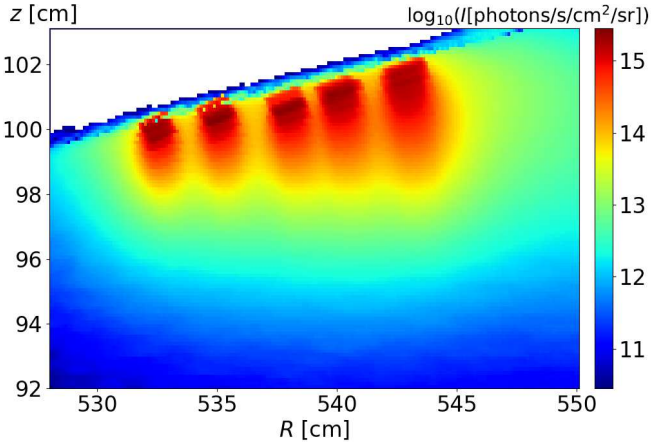

Figure 2: Synthetic image of the 706.5 nm line intensity in the poloidal plane at the gas nozzle location, medium plasma density case. Colorbar corresponds to $\log_{10}(I[\text{photons/s/cm}^2\text{/sr}])$. The virtual camera is placed 1 m toroidally away from this plane and views perpendicularly onto it. T_e and n_e in the plane of emission are displayed in figure 3. Five beams, injected simultaneously at the upper divertor (interface between white and blue region), propagate downwards. Thermal spread in beam source, meta-stable states [13] and p-He elastic scattering [29] are included, no recombination. Beam parameters are taken from [6, 34]. Particle flux is $\dot{N} = 1.5 \times 10^{19}$ s^{-1} per beam.

a low and medium density case. For figure 2, the 'medium density' case was used. A wider plasma density scan up to envisioned future 'high density' plasma conditions, with $n_e \gtrsim 10^{14}$ cm^{-3} foreseeable at W7-X [16], was left to future work. Here we focus on the status of synthetic diagnostic tools as such.

The elastic p-He scattering allows to take account of collisional beam widening (see section 8) and heating of beam particles. Also present in all results shown in this paper are the transport effects of the two meta-stable states of the He atom, namely the 2^1S and 2^3S singlet and triplet states, which are fully retained as separate helium species with own transport equations.

Following the experimental parameters by *Barbui et al.* [6], the He beams were simulated with a particle flux of 1.5×10^{19} s^{-1}. In the 'medium density case' this leads to a local He density of up to 6×10^{13} cm^{-3}. Hence, the conditions are near the onset of both local n_e perturbations due to the He puff and helium line opacity effects. In the experiment no perturbation was observed [6], therefore these effects are omitted here. They can be taken into account, though, by including the He puff in the calculation of the plasma background and reactivating the radiation transport module.

4. Synthetic spectroscopy model

The central quantity for the diagnostic is the spatial profile of a volumetric emissivity (emitted photons per unit volume and time) $\varepsilon(\boldsymbol{r}, p \to q) = n(\boldsymbol{r}, p)A(p \to q)$. It is given for a transition from an atomic state $p = n^{2S+1}L$ into a lower state q. The states are determined by the principal quantum number n, spin S and angular momentum quantum number L. The local emissivity is equal to the population density $n(p)$ of the excited state p times spontaneous decay rate A for the observed transition. The local population density depends linearly on the densities of donor states (the local ground and meta-stable He atom densities found from the transport simulation) and it can vary with local values of T_e and n_e due to rapid collisional-radiative mixing amongst the excited states. These same dependencies arise also for the emissivity. The purpose of the embedded CR model is to connect $n(\boldsymbol{r}, p)$ to T_e and n_e and simultaneously (and consistently) to provide the transport mean free pathes for the thermal beam particle simulation.

In a real experiment, information about plasma parameters T_e and n_e has to be extracted from line-of-sight (LOS) integrated, or "side-on" light intensity I, a non local

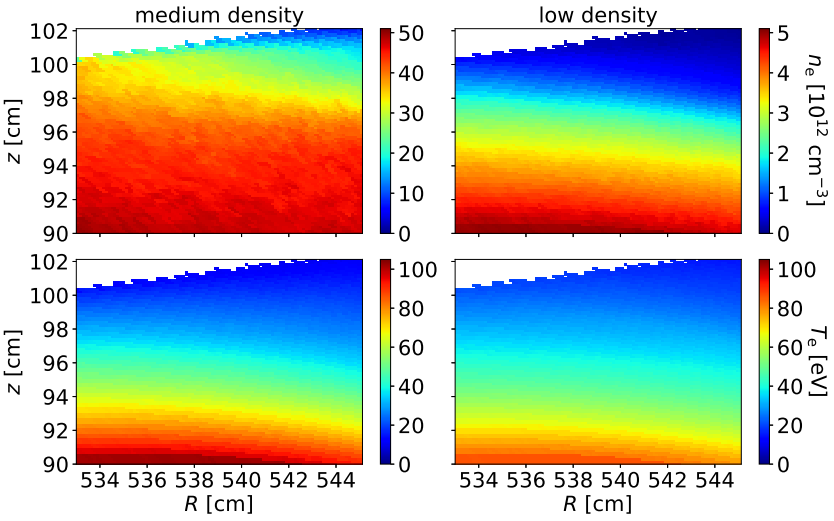

Figure 3: Background n_e [10^{12} cm^{-3}] (top) and T_e [eV] (bottom) in front of the W7-X upper divertor, as generated by EMC3-EIRENE [35], depicted in the poloidal plane at the He nozzles' location. Medium density case with $P_{SOL} = 10$ MW heating power and $\langle n_e \rangle_{LCFS} = 5 \times 10^{13}$ cm^{-3} upstream density (left), low density case with $P_{SOL} = 1$ MW and $\langle n_e \rangle_{LCFS} = 5 \times 10^{12}$ cm^{-3} (right). Other input parameters are the same as in [36, table 1]. T_e-profile remains similar, but n_e changes by an order of magnitude. White region is behind the divertor.

observable. In absence of re-absorption, light scattering or reflections it is equal to the line-integral of emissivity ε along the camera's pixel LOS (the difference to view cone integrals is discussed in [27, appendix]),

$$I(\boldsymbol{r}) = \frac{1}{4\pi} \int_{\mathrm{LOS}} \mathrm{d}s\, \varepsilon(s) = \frac{1}{4\pi} \sum_{m=1}^{N} \Delta s_m \varepsilon_m, \quad (1)$$

which becomes a sum if data are represented on a fine discrete grid (as in EIRENE). ε_m is then the emissivity in grid cell m, already integrated over (Doppler) spectral line profile, and Δs_m is the length of the segment of the line of sight across this cell. The factor $1/4\pi$ arises from assuming isotropic emission.

In beam emission spectroscopy one measures the light intensity at an angle, preferentially perpendicular, to a narrow beam with diameter Δs. Therefore, the line integration effect may become negligible, hence

$$I(\boldsymbol{r}) = \frac{1}{4\pi} \int_{\mathrm{LOS}} \mathrm{d}s\, \varepsilon(s) \approx \frac{\Delta s}{4\pi}\, \varepsilon(\boldsymbol{r}), \quad (2)$$

with the focal point $\boldsymbol{r}$. This is, of course, not always achievable: as seen above, especially in denser plasmas the beam width tends to increase along the beam axis.

Commonly, three spectral lines are observed in He BES. This allows to extract information about both T_e and n_e from line intensity ratios. Ratios are often preferred over absolute intensities since to a large part calibration uncertainties cancel. Additionally, line intensity ratios are better localized (relaxed to local collisional radiative equilibrium) than absolute line intensities [23], thus better justifying a quasi-stationary CR model approach for their interpretation. A common choice is

$$\begin{aligned} R_{T_e} &= \frac{I(728.1\,\mathrm{nm})}{I(706.5\,\mathrm{nm})} \approx \frac{\varepsilon(728.1\,\mathrm{nm})}{\varepsilon(706.5\,\mathrm{nm})} \\ &= \frac{n(3^1S) A(3^1S \to 2^1P)}{n(3^3S) A(3^3S \to 2^3P)} \text{ and} \quad (3) \\ R_{n_e} &= \frac{I(667.8\,\mathrm{nm})}{I(728.1\,\mathrm{nm})} \approx \frac{\varepsilon(667.8\,\mathrm{nm})}{\varepsilon(728.1\,\mathrm{nm})} \\ &= \frac{n(3^1D) A(3^1D \to 2^1P)}{n(3^1S) A(3^1S \to 2^1P)}. \quad (4) \end{aligned}$$

We denote emissivity ratios by $R^{\varepsilon}_{T_e/n_e}$. It is important that the measured line intensity ratios are equal to emissivity ratios only if locality of emission (2) holds. For the more general case we shall introduce for each line of sight (or pixel) a correction factor

$$G(\mathrm{LOS}) = \frac{\int \mathrm{d}s\, \varepsilon_1(s)}{\int \mathrm{d}s\, \varepsilon_2(s)} \Big/ \left(\frac{1}{\int \mathrm{d}s} \int \mathrm{d}s\, \frac{\varepsilon_1(s)}{\varepsilon_2(s)} \right) \quad (5)$$

and write $R_{T_e/n_e} = G_{T_e/n_e} \cdot R^{\varepsilon}_{T_e/n_e}$. The expression in the denominator of G is a line-

of-sight averaged emissivity ratio − a local emissivity ratio can be used alternatively in the definition. A local CR model (without transport terms) is only applicable for a quantitative interpretation of measurements if G is known or can be assumed to be ≈ 1 by other considerations, since it only describes $R^{\varepsilon}_{T_\mathrm{e}/n_\mathrm{e}}$. Otherwise, in case of additional symmetries one may apply Abel inversion [9] or, more generally, tomographic reconstruction to obtain directly the emissivity profile. Such symmetries are not necessarily given in complicated magnetic plasma boundary configurations as for example in stellarators. There, instead, these correction factors follow from the post-processing line integration procedures in EIRENE, in 3D applications see e.g. [25] for TJ-II, or [26, 27] for W7-X. The correction is even more important for He BES, since in measured line ratios (compared to line intensities) LOS averaging happens both in the numerator and denominator. Because both are correlated, the averaging must not cancel out, leading to an additional non-local bias to both T_e and n_e above or below the actual LOS average, depending on the actual $\varepsilon(s)$ profile. This is investigated in more detail in section 10.

For fast interpretation of experimentally observed line ratios R^{exp}_I, it is further necessary to find the inverse functions $T_\mathrm{e}(R_{T_\mathrm{e}}, R_{n_\mathrm{e}})$ and $n_\mathrm{e}(R_{T_\mathrm{e}}, R_{n_\mathrm{e}})$ for measured $R^{\mathrm{exp}}_{T_\mathrm{e}/n_\mathrm{e}}$. Typically [23, 13], this is done by finding $R^{\varepsilon}_I(T_\mathrm{e}, n_\mathrm{e})$ from the CR model such that the deviation

$$D(T_\mathrm{e}, n_\mathrm{e}) = \sum_{I=T_\mathrm{e},n_\mathrm{e}} \left(1 - \frac{R^{\mathrm{exp}}_I}{R^{\varepsilon}_I(T_\mathrm{e}, n_\mathrm{e})}\right)^2 \qquad (6)$$

is minimized. Without additional constrains, e.g. from other measurements, this is reliably only possible under certain conditions, e.g. quasi-stationarity [12]. On the other hand, in the forward calculation of $R_{T_\mathrm{e}/n_\mathrm{e}}(T_\mathrm{e}, n_\mathrm{e})$ by the synthetic diagnostic such constrains can be largely relaxed and more effects can be taken into account computationally. This then allows to test their role and to estimate their possible propagation to real experimental applications of the interpretation procedure.

Finally, the local functions $R^{\varepsilon}_{T_\mathrm{e}}(T_\mathrm{e}, n_\mathrm{e})$ and $R^{\varepsilon}_{n_\mathrm{e}}(T_\mathrm{e}, n_\mathrm{e})$ for any line ratio are mainly determined by atomic data. For the present analysis, the EIRENE helium database (mainly for electron collisions) was updated from Fujimoto's [28] to GCRM [13] with some more details also with regard to the application to BES given in the next section.

5. Collisional-radiative model, atomic data and their handling

The basic concept and structure of Fujimoto's original CR model from 1979 [28] has been retained, including its meta-stable resolved features with the ground and two meta-stable states each carrying their own "train" of further excited helium atoms and its local thermal equilibrium (LTE) limit closure above principal quantum number $n = 20$. Summarizing the recent helium atomic data set in the revised CR code by Goto [13], it contains

- in total 65 different n, l resolved atomic states in the singlet and triplet system ($n \leq 26$),
- two formulations, with either resolved or equilibrated ("CR-condensed") meta-stable states 2^1S and 2^3S,
- three-body, radiative and dielectronic recombination,
- electron collision cross sections for ionization and excitation from the internationally evaluated database (under IAEA

guidance), summarized by Ralchenko *et al.* [14],

- precise spontaneous transition rates and
- singlet-triplet wave function mixing due to spin-orbit interaction by Drake [15].

The main differences to the previous EIRENE helium default model [28] are the revised electron collision cross section data, whereas all features of the first three bullets are kept the same as in all code distributions before, e.g. as applied earlier in 3D helium emission simulations for the TJ-II stellarator [7]. A more detailed discussion of the underlying atomic cross section databases and propagation of differences between them to the BES interpretation results is given in [22].

The CR model allows to express the local excited state density in two different forms, referred to simply as formulation I or formulation II by Fujimoto and in EIRENE (nowadays mostly: "meta-stable resolved" and "meta-stable condensed" formulation, resp.),

$$n(p) = r_0(p) n_\mathrm{e} n(\mathrm{He}^+) + r_1(p) n_\mathrm{e} n(1^1S) + r_2(p) n_\mathrm{e} n(2^1S) + r_3(p) n_\mathrm{e} n(2^3S) \quad (7)$$

or

$$n(p) = R_0(p) n_\mathrm{e} n(\mathrm{He}^+) + R_1(p) n_\mathrm{e} n(1^1S) \quad (8)$$

[13, eqs. (21) and (29)].

Population coefficients r and R depend on T_e and n_e via the mix of electron collisional and radiative coupling between all electronic states. The meta-stable condensed "formulation II" rests on only two excited state populations which are in collisional-radiative equilibrium with the ground state or with the He^+ ion, respectively. Formulation I retains, additionally, the two meta-stable states 2^1S and 2^3S as further independent species with their own transport equations and own excited state populations in the forward EIRENE simulation.

In today's fusion experiments, one is mostly concerned with the triplet meta-stable 2^3S [11, 16], since 2^1S typically relaxes fast enough [37]. The singlet meta-stable 2^1S is included in GCRM, because this code as well as its predecessor model [28] have been and still are also intended for application to a positive-column plasma with quite distinct parameters.

Spatial profiles of $n(\mathrm{He}^+)$, $n(1^1S)$, $n(2^1S)$ and $n(2^3S)$ are obtained by EIRENE, using again the CR model and Monte Carlo integration of the four coupled kinetic transport equations, on a 3D EMC3 computed plasma state. In a real experiment, these four densities are typically unknown. The interpretation of the diagnostic signal essentially relies on formulation II (8) and neglects recombination ($n(\mathrm{He}^+) = 0$) [23], so only the helium ground state $n(1^1S)$ density remains as relevant donor state for emission. Inserting this reduced form of (8),

$$n(p) = R_1(p) n_\mathrm{e} n(\mathrm{He}\, 1^1S),$$

into the emissivity ratios expressions (3)-(4) for the upper state helium densities, leads to complete cancellation of the neutral $n(1^1S)$ density dependence from them.

Possible procedures to relax the limitations resulting from formulation II as compared to formulation I have been proposed by [11, 8], but it is still common practise to apply meta-stable unresolved CR models to BES interpretation. We will come back to this issue in section 9.

Using GCRM (formulation II), we display such emissivity ratios $R^\varepsilon_{T_\mathrm{e}}(T_\mathrm{e}, n_\mathrm{e})$ and $R^\varepsilon_{n_\mathrm{e}}(T_\mathrm{e}, n_\mathrm{e})$ in a contour plot in figure 4. They allow a rough estimate of $T_\mathrm{e}(R_{T_\mathrm{e}}, R_{n_\mathrm{e}})$ and $n_\mathrm{e}(R_{T_\mathrm{e}}, R_{n_\mathrm{e}})$, e.g. $T_\mathrm{e}(0.5, 6) \approx 50$ eV and $n_\mathrm{e}(0.5, 6) \approx 15 \times 10^{12}$ cm^{-3} (marked in red).

The CR model is built from reaction rate coefficients. When calculating electron

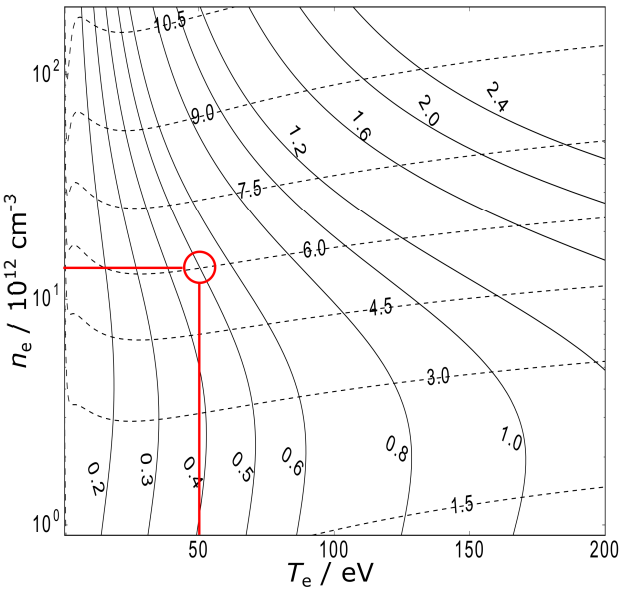

Figure 4: Emissivity ratios computed from GCRM [13] at $B = 2.5$ T, formulation II, $n(\mathrm{He}^+) = 0$. Solid line - $R^{\varepsilon}_{T_e} = \varepsilon(728.1\,\mathrm{nm})/\varepsilon(706.5\,\mathrm{nm})$, dashed - $R^{\varepsilon}_{n_e} = \varepsilon(667.8\,\mathrm{nm})/\varepsilon(728.1\,\mathrm{nm})$. Red mark - see text.

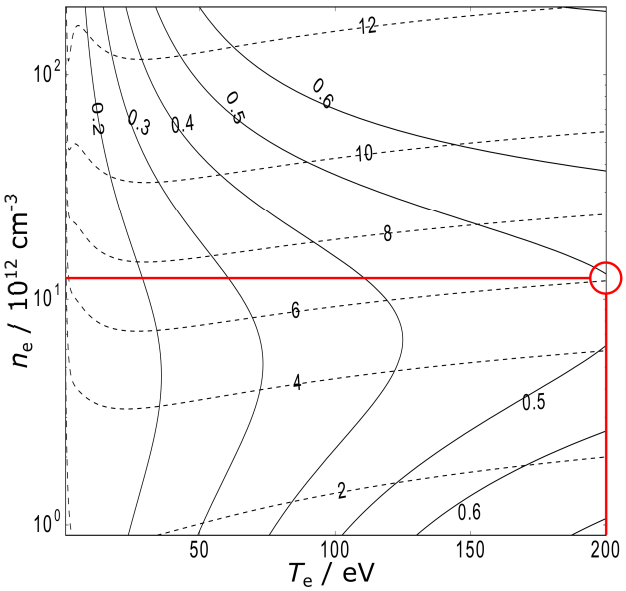

Figure 5: Emissivity ratios with GCRM limited to 29 states ($n \leq 5$). Notice the shifted red mark compared to figure 4.

impact transition rate coefficients from the collision strength fits from [14] by numerical integration, it is important to note that some extrapolation to very low collision energies (below 0.1 eV) was required to eliminate spurious behaviour of these fits in this extreme low energy range [22]. In the mentioned database, this concerns l-mixing transitions with very small threshold energies, below 0.1 eV − cross section calculations by the CCC-89 method [38] had only been performed above 0.1 eV [39]. Care is needed when applying the CR model at $T_e \ll 10$ eV. However, at such low T_e little detectable light is emitted [6, 16], so that this does not concern the interpretation of the He BES diagnostic.

Theoretically calculated data for helium, e.g. by the convergent-close-coupling (CCC) [40] or R-matrix with pseudo-states (RMPS) [41] methods, generally appear to be very reliable today. For example a long lasting discrepancy between theory and experiment for the ionization cross section from the helium 2^3S meta-stable state was recently finally resolved by new measurements, in favour of the theoretical data [42].

The atomic data in this work were made publicly accessible at the HYDKIN online database [43], and can be used with the online solver [37] for 0D and 1D plasma kinetics simulations.

6. Cut-off problem

The cut-off problem refers to the natural question: how many energy eigenstates must be really considered? While the Hilbert space of energy eigenstates of an isolated atom in vacuum is infinite, the set of ordinary differential equations in a CR model in a plasma environment is finite. The reason are "continuum lowering effects" due to surrounding plasma electrons and ions [44, 45, 46, 47]. Yet the proper cut-off depends on local plasma conditions, the particular ion, and it is

still often chosen very differently [23, 12, 13, 11] due to practical considerations.

Precise and internationally evaluated *ab initio* cross section calculations are only available for lower excited states ($n \leq 4$ in [14]). Here we point out the potential importance of much higher excited states (up to $n = 26$ in the Goto-Fujimoto model) and hence collisional radiative cascading to and from them: if we reduce the maximum considered electron shell from $n = 26$ to $n = 5$ (as e.g. in the also fairly wide distributed earlier Brix-Fujimoto CR model [23]), figure 4 turns into figure 5.

Naturally, the discrepancy increases with temperature, since the population of high excited states rises. Electron temperatures obtained in this way (from figure 5) may be wrong by up to a factor of 4 (see the red mark). The difference between figure 4 and figure 5 reduces gradually when the number of included energy eigen-states is increased stepwise back to $n = 26$.

The fixed cut-off at $n = 26$ in GCRM is somewhat artificial due to practical considerations [28, p. 443], but well justified. Importantly, it is preceded by a LTE cut-off n_0, above which the population is *a priori* assumed to be in local thermal equilibrium. As shown e.g. in [44, chapter 5.4.2], the radiative decay probability decreases with n as $A \propto n^{-5}$, while electron collision frequencies increase with n. Hence, a principal quantum number n_0 can be defined, beyond which the electronic population satisfies LTE according to the Saha-Boltzmann equation. According to [44, chapter 5.4.2], a rough estimate for n_0 (in the hydrogenic approximation) would be

$$n_0 \simeq z \left(\frac{10^{18}\ \mathrm{cm}^{-3}}{n_\mathrm{e}} \right)^{1/7} \left(\frac{T}{z^2 Ry} \right)^{1/14}, \qquad (9)$$

with the Rydberg energy $Ry = 13.6$ eV, temperature T expressed in eV and $z = 1$ for neutral helium [44, equation 5.1.13]. For $T_\mathrm{e} \in [2, 200]$ eV and $n_\mathrm{e} \in [10^{12}, 10^{14}]$ cm^{-3}, $n_0 < 9$. To be applicable to a broader parameter range, in GCRM $n_0 = 20$.

On the other hand, there exists a strict physical cut-off n_m, beyond which excited states are "pressure ionized" [47]. There are many models and a vast literature discussing the maximum principal quantum number [46]. Most of them, however, agree that the continuum lowering (in Gauss units) has the form

$$\Delta E_m = \frac{\zeta e^2}{R^*}, \qquad (10)$$

with the number of free electrons per ion being $\zeta = 1$ in hydrogen plasmas. Bound states must have energies $|E(n)| > \Delta E_m$. A simple estimate is obtained by setting $R^* = R_\mathrm{i} = n_\mathrm{i}^{-1/3}$, the ion sphere radius [47]. Approximating high excited states as hydrogenic, $|E(n)| = Ry/n^2$, for $n_\mathrm{i} = n_\mathrm{e} \in [10^{12}, 10^{14}]$ cm^{-3} we obtain

$$n_m = \frac{\sqrt{Ry}}{e} n_\mathrm{e}^{-1/6} \in [97, 45]. \qquad (11)$$

More sophisticated models predict an even significantly lower n_m [46], e.g. $n_m \lesssim 21$ according to [47, eq. (3.4.6)]. In GCRM, $n_m = 26$. This might explain why the inclusion of high Rydberg states with up to $n = 500$ by [11] deteriorates the agreement with other models and measurements.

Currently, higher excited states with $n > 4$ can be only included in GCRM by applying semi-classical scaling relations [13] or, for even higher n, the hydrogen approximation [28]. Consequently, regarding the demonstrated sensitivity of BES results to these upper states, one can conclude that more precise theoretical data for them are required, should there be indications that the scalings in use are inappropriate.

7. Singlet-triplet state mixing

In GCRM, reaction rates vary with the magnetic field due to the singlet-triplet wave function mixing [13]. With the mixing coefficient $\omega(B)$ from [15], e.g. the singlet ionization rate coefficient becomes

$$S_{\rm iz}(n^1L) = (1-\omega^2)S^0_{\rm iz}(n^1L) + \omega^2 S^0_{\rm iz}(n^3L), \quad (12)$$

where $S^0_{\rm iz}$ is the "pure" coefficient at $B = 0$, without mixing. The $B-$field dependence propagates through the CR model up to emissivity ratios, as shown in figure 6, so that the interpretation of spectroscopic measurements requires also considering the local magnetic field at the point of emission.

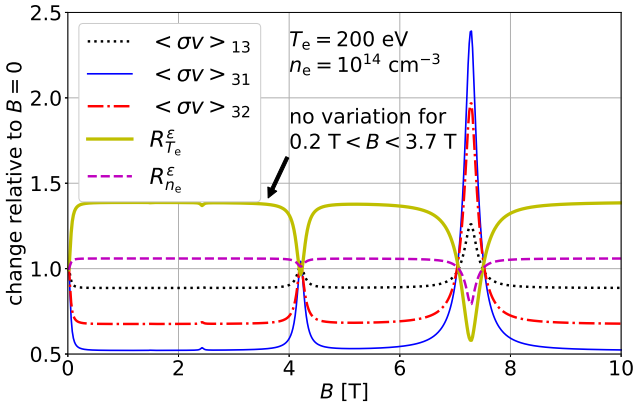

Figure 6: Dependence of coupling rate coefficients amongst ground and meta-stable states (see text), and of emissivity ratios (3) and (4) on the magnetic field, normalized to their value at 0 tesla.

The $B-$field dependence of the triplet meta-stable state 2^3S coupling rate coefficients $\langle\sigma v\rangle$, required for the meta-stable resolved modelling of the beam propagation, is also shown. These rate coefficients are the production and loss rates of the 2^3S state, to and from the ground and singlet meta-stable state: $\langle 13\rangle \hat{=} 1^1S \rightarrow 2^3S$, $\langle 31\rangle \hat{=} 2^3S \rightarrow 1^1S$, $\langle 32\rangle \hat{=} 2^3S \rightarrow 2^1S$. This suggests that also the meta-stable helium transport in the plasma depends on the magnetic field. However, other effective rate coefficients are affected much less, so that the overall helium density may remain unchanged.

Notice the resonance-like behaviour with peaks at 0, 2.4, 4.2 and 7.3 tesla. Although the effect of the mixing is highest for $T_e > 50$ eV and $n_e \gtrsim 10^{14}$ cm^{-3}, the peaks positions remain unchanged. The insignificance of the very small peak at 2.4 T can be used as argument to omit the explicit magnetic field dependence for the range $B \in [0.2, 3.7]$ T. Therefore, for medium B-field fusion experiments like W7-X (with magnetic field strength in the 1 to 3 Tesla range), a constant correction of all rate coefficients is sufficient.

The newly added precomputed helium atomic data set for EIRENE contains this constant correction factor. However, the same data set may therefore be inappropriate for $B \approx 0$ T and $B > 3.7$ T (e.g. the high field Alcator C-Mod tokamak). In future, the helium CR code will therefore be directly included into EIRENE, like it is the case already for hydrogen [30, 31], rather than relying on precomputed (tabulated or fitted) data, to take the magnetic field (and potentially further dependencies such as radiation trapping) explicitly into account.

We stress that particular attention to the magnetic field dependence will be required at future fusion experiments, such as ITER: when the magnetic field strength B crosses the 7.3 T resonance at the place of measurement, this dependency cannot be neglected in the interpretation of helium beam or passive spectroscopic measurements.

8. Beam opening angle estimation

To quantify the collisional beam widening due to elastic p-He scattering, we define the half angle of beam spread α as the effective mean

squared emission angle:

$$\alpha^2 = \frac{1}{N}\sum_{k=1}^{N}\alpha_k^2,\ \cos(\alpha_k) = \boldsymbol{e}_\mathrm{b}\cdot\frac{\boldsymbol{r}_{k,i}-\boldsymbol{r}_{k,0}}{|\boldsymbol{r}_{k,i}-\boldsymbol{r}_{k,0}|}. \quad (13)$$

The unit vector $\boldsymbol{e}_\mathrm{b}$ marks the beam axis and the sum is formed over N "analog" He Monte Carlo test particles (no statistical weighting applied here). $\boldsymbol{r}_{k,0}$ is their entrance location (the nozzle) and $\boldsymbol{r}_{k,i}$ is the point where they are ionized. α_k is the angle by which the ionization point of particle k deviates from the beam axis.

Without the elastic scattering process, the mean value of α_k is zero by construction and the mean squared α is determined solely by the angular particle source distribution, which we have set such that $\alpha = 20°$, according to [34]. Due to p-He collisions, however, α becomes wider, 24° in the low density case (figure 3, right). In the medium density case (figure 3, left), $\alpha \approx 35°$. With elastic scattering the beam is also localized visibly closer to the divertor target in figure 7. Apparently the ionisation mean free path enhancement due to heating up of beam particles by elastic scattering is over-compensated by the increased density effect to reduce the mean free path again. At even higher densities and smaller temperatures, as expected in later experimental campaigns at W7-X, the localization may become even more pronounced.

9. Diagnostic evaluation algorithm

The accuracy of He BES at W7-X, and in other fusion experiments as well, is limited due to four reasons:

(a) the complicated 3D geometry, which makes the hardware measurement set up and signal interpretation more difficult,

(b) the not fully assessed high density, low temperature parameter range [16] in detached divertor states,

(c) not completely CR-equilibrated metastable states, i.e. finite relaxation times (and hence ballistic transport effects),

(d) additional, notably heavy particle atomic interactions, not taken into account by the CR model [12, 8].

In complex magnetic topologies it is more difficult to account for line-of-sight integration effects. Complexities are further introduced e.g. by beam broadening due to heavy particle interactions, although we believe that the dominant process (elastic He-p scattering) has now properly been taken into account (see section 8). At $T_\mathrm{e} < 10$ eV, He line emission is weak [6, 16].

To address all these challenges, we have used the synthetic He beam diagnostic as e.g. implemented in EIRENE. More precisely, the algorithm for the evaluation of internal consistency of helium BES is:

(i) Simulate the helium beam with a code such as EIRENE for a given plasma state, including transport effects in metastable states, elastic scattering and other relevant interactions.

(ii) Apply the same local collisional-radiative model implicitly used in (i) to obtain local emissivity patterns in 3D.

(iii) Construct synthetic camera views with line-of-sight integrals, pixel by pixel.

(iv) Reconstruct the plasma parameters n_e and T_e from the synthetic views, from an experimentally accessible camera position, again using the same helium CR model, and compare with the (known) plasma fields from step (i).

(v) Improve the interpretation step (iv) (using more line ratios, different camera positions, etc...) if necessary.

As an example, we consider here the issue of not sufficiently fast meta-stable state relaxation times ('reason (c)'). They introduce an explicit dependence of excited state populations on non-equilibrated meta-stable state densities according to (7), which does not cancel in the line intensity / emissivity ratios (3)-(4). In step (i) of the algorithm, it is straight forward to compute not only $n(1^1S)$, but also $n(2^1S)$ and $n(2^3S)$ using formulation I in EIRENE. In the experiment, however, these densities are usually unknown, so that experimental BES signal interpretation typically relies on formulation II and neglects recombination (see section 5). To quantify the effect of this, we will use these approximations in step (iv) of the algorithm.

To separate, computationally, these equilibration time scale effects from purely geometrical effects, it is possible to evaluate the emissivity in the poloidal plane directly (skipping step (iii) in the algorithm). Using synthetic camera pictures like figure 2, on the other hand, allows to also quantify the effect of LOS integration, i.e. the correction factor G_{T_e/n_e} – see section 10.

For a single beam, taking explicitly into account meta-stable states according to (7) (formulation I) and elastic p-He scattering, the emissivity of the 706.5 nm line is displayed in figure 7 for both density cases described in section 3, figure 3. Then we construct the emissivity ratios (acting as 'measured' line ratios) according to (3) and (4). Finally $T_e(R_{T_e}, R_{n_e})$ and $n_e(R_{T_e}, R_{n_e})$ are found by minimizing $D(T_e, n_e)$ in (6), using helium CR model data obtained with (8), formulation II.

The initial (figure 3) and reconstructed temperature profiles are displayed in figure 8 for both density cases. The Monte Carlo (MC) noise is due to the estimation of $n(1^1S)$, $n(2^1S)$ and $n(2^3S)$ by a finite number N of test particles. Statistical (MC) noise effects are pronounced further away from the gas inlet, where only few test particles reach. No attempt has been made so far to reduce statistical errors by any of the conventional variance reduction methods available in EIRENE, since here we have not been limited by available CPU time. With enough test particles, the initial profile of the medium density case (left) can be exactly reconstructed for $z \in (94, 101)$ cm. Outside this region, no signals were detected (see figure 7). In the low density case (right), the beam penetrates deeper into the plasma, allowing precise T_e reconstruction up to 10 cm away from the divertor plates. However, directly in front of the divertor the reconstruction fails. This is due to the aforementioned finite meta-stable equilibration times, the more precise formulation I used in the forward simulation, distinct from the simpler formulation II in the reconstruction phase. The reconstruction of the density profile, however, is not affected.

The He BES interpretation therefore has to be modified and refined in this parameter range. Possible solutions being pursued are fitting of meta-stable population densities [8] or calculating them from the completely "time dependent CR model" [11]. Using the first approach [8] in step (iv) of our algorithm, we could verify its unambiguity. The second approach relies on a number of assumptions about the helium beam propagation, to convert the time parameter in a space-homogeneous CR model into a (1D) space coordinate for the (inherently stationary) BES interpretation: e.g. mono-energetic and unidirectional helium atoms are assumed in the beam in this procedure. By contrast, EIRENE allows us to simulate realistic thermal beam spread into a precomputed 3D plasma.

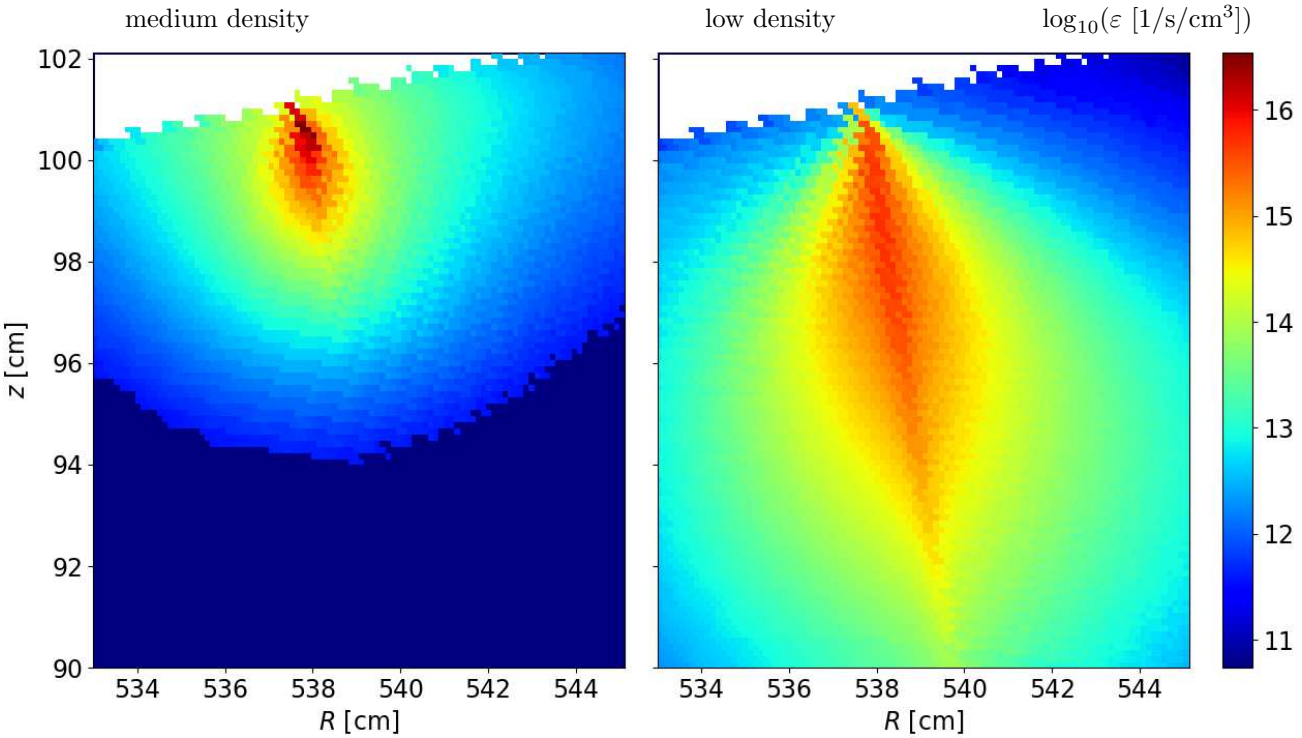

Figure 7: Decadic logarithm of the 706.5 nm line emissivity, $\log_{10}(\varepsilon\ [1/\mathrm{s/cm^3}])$, in the poloidal plane. Left – $P_{\mathrm{SOL}} = 10$ MW and $\langle n_\mathrm{e}\rangle_{\mathrm{LCFS}} = 5 \times 10^{13}$ cm^{-3}, right – $P_{\mathrm{SOL}} = 1$ MW and $\langle n_\mathrm{e}\rangle_{\mathrm{LCFS}} = 5 \times 10^{12}$ cm^{-3}. p-He elastic scattering included, formulation I, recombination neglected. Contrast limited to 10^5, $\dot{N} = 1.5 \times 10^{19}$ s^{-1}.

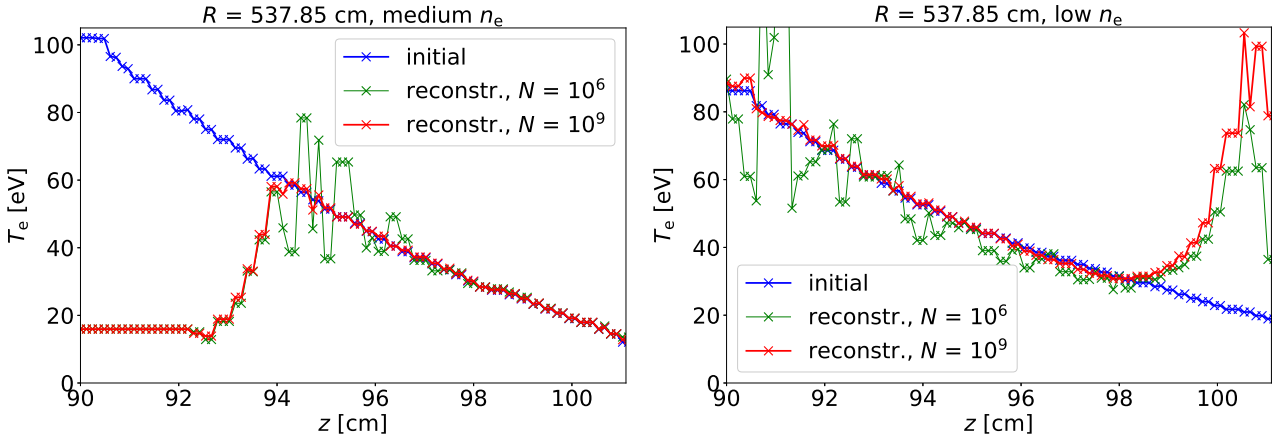

Figure 8: T_e reconstruction from the synthetic He beam diagnostic along vertical axis z (divertor at ≈ 101 cm), according to the algorithm (see text). Left – medium density profile case, right – low density case (see figure 3). Poloidal plane and radius fixed. N is the number of MC test particles in the beam simulation.

Thereby, meta-stable states transport is taken into account explicitly, while all other excited states remain stationary.

10. Line-of-sight integration errors

In the previous paragraph we have introduced an algorithm for the numerical evaluation of the He BES diagnostic. We then verified that finite meta-stable relaxation times must

be taken into account at low densities, e.g. by formulation I. To separate that from geometrical effects, we skipped step (iii) in the algorithm. In this section, by contrast, we will compare local emissivity ratios from step (ii) with line ratios from step (iii) to quantify the necessary LOS correction factor G_{T_e/n_e}, introduced in section 4.

We note, however, that in particular in 3D configurations purely numerical "discretisation" errors due to finite grid resolution in the vicinity of the He beam may also be relevant. In our current work, we have achieved a resolution of ∼3 mm in the poloidal plane. Due to limited computational resources, toroidal resolution was limited to 0.5° though, corresponding to ∼5 cm long (curved) grid cells. A finer grid will have to be approached for a more precise determination of G(LOS).

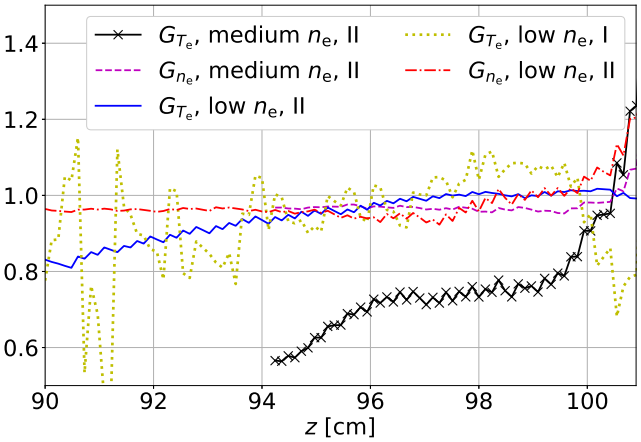

Figure 9: Line-of-sight correction factor G_{T_e/n_e} for both density and temperature, in the low and medium density cases from figure 3. A profile along the vertical axis with fixed $R = 537.85$ cm is shown, as in figure 8, and emissivity ratios $R^{\varepsilon}_{T_e/n_e}$ are calculated in the same plane as in figure 3 or 7. Line intensity ratios R_{T_e/n_e} are calculated from LOS integrated intensities, in the same way as in figure 2. II stands for formulation II, meaning equilibrated meta-stable states were assumed. At low n_e this assumption breaks down for R_{T_e} close to the divertor, as in figure 8 − therefore also a formulation I calculation is shown, but with only 10^6 MC particles.

For the two plasma density cases (figure 3) regarded in this work, G_{T_e/n_e} is displayed in figure 9 along the vertical axis in the same poloidal plane. Emissivity ratios were not LOS averaged here. We retain formulation II where possible, but at low density also show G_{T_e} in formulation I (both R_{T_e} and $R^{\varepsilon}_{T_e}$ from I), since it becomes necessary close to the divertor according to figure 8. The MC noise in formulation I deep in the plasma is irrelevant, since formulation II is also valid there. Medium density G profiles are only shown up to $z \approx 94$ cm since He does not reach deeper there. The numerical results are summarized in table 1.

Table 1: Average and maximum values of $|G-1|$ from figure 9. Maximum for G_{T_e} at low n_e in formulation I is given in front of the divertor, ignoring MC noise deep in the plasma.

	$< \lvert G-1 \rvert >$	$\lvert G-1 \rvert_{\max}$
G_{T_e}, med. n_e, II	25.8%	43.6%
G_{T_e}, low n_e, II	5.8%	19.0%
G_{T_e}, low n_e, I	10.5%	31.8%
G_{n_e}, med. n_e, II	3.3%	6.7%
G_{n_e}, low n_e, II	4.3%	20.1%

We can observe the most pronounced deviation from 1 for G_{T_e} in the medium density case, which would lead to an underestimation of T_e in the experiment. At low n_e, $|G_{T_e} - 1|$ is large only deep in the plasma. $|G_{n_e} - 1|$ is generally less significant, but large deviations occur close to the divertor. In the divertor region, all $G \gtrsim 1$ in formulation II, while in formulation I $G_{T_e} < 1$.

The dependence of G_{T_e/n_e} on ε(LOS) profiles, hence not only T_e and n_e but also their profiles in a non trivial way, might make it difficult to correct experimental measurements − but further investigation of such possibilities is required.

We note that according to the above

observations, LOS averaging might be another explanation for a systematic underestimation of T_e compared to other diagnostics [12]. This should be taken into account when comparing the application of different atomic data to the experiment [11] or adjusting the atomic data [16]. However, our analysis needs to be repeated with a higher toroidal grid resolution, for more plasma backgrounds and different camera locations.

11. Conclusions

We have extended the synthetic BES diagnostic options in the 3D edge code package EMC3-EIRENE to facilitate application to a wider range of spectral emission lines, on the basis of a set of publicly exposed and internationally evaluated atomic collision cross sections. A closed loop of forward transport simulations and backward reconstruction for 3D edge plasma temperatures and densities, using identical atomic models in both, is established.

Flexible placement of a virtual camera allows the quantification of line-of-sight integration effects in full 3D, and hence their computational separation and elimination from real BES in W7-X by application to typical magnetic configuration and edge plasma conditions.

By explicitly calculating the transport of meta-stable He states and their emission we can verify when it is applicable to use the common assumption of them being in equilibrium with the ground state, and when not. Showing their individual contributions, we also clearly separate the effects of meta-stable states and line-of-sight integration on the reconstruction of plasma parameters by He BES.

Accounting for additional (heavy particle) collision processes in the forward transport simulation we can assess propagation of their relevance into the helium BES signal processing. We have shown that elastic p-He scattering provides a significantly enhanced beam divergence, in particular in the envisioned high density hydrogen plasma conditions in the W7-X divertor.

The GCR model takes singlet-triplet wave function mixing into account, resulting in an explicit dependence of BES signals on the magnetic field strength. We have shown that for 0.2 T $< B <$ 3.7 T, as at W7-X, this dependence can be accounted for by just a constant correction factor on the (T_e, n_e)- dependent CR data. However, this constant correction factor approximation is not sufficient for higher B-field machines, such as ITER.

We have revisited the cut-off problem, demonstrating the importance of cascading to and from excited energy eigenstates with $n \gg 4$. For these states only physically based cross section scaling relationships are available today. On the other hand, we argued that a cut-off at $n < 30$ is justified and necessary, so that high Rydberg states can and should be excluded from the CR model.

We find the determination of n_e by He BES to be generally significantly more robust then T_e. Throughout our studies, it is much less influenced by line-integration, meta-stable states, singlet-triplet wave function mixing or cut-off in the CR model.

In future BES applications, moving further towards detached divertor plasma conditions ($n_e \gtrsim 10^{14}$ cm^{-3}), the syntectic diagnostic loop presented here allows to study the effects from volumetric recombination processes. The role of further heavy particle collisions can be evaluated. Including other spectral lines and absolute line intensities (proposed by [16]) can be assessed computationally as a

way to improve the diagnostic. A direct implementation of the He CR model used here into EIRENE (without prior parametrization in the multi-dimensional parameter space) is currently carried out, facilitating then explicit consideration of the magnetic field, as well as the so far neglected opacity effects and photon reflection at wall surfaces.

Acknowledgments

We are thankful for valuable discussions with Vladislav Kotov, Felix Reimold and Yuri Ralchenko.

The authors gratefully acknowledge the computing time granted through JARA-HPC on the supercomputer JURECA [48] at Forschungszentrum Jülich.

This work has been carried out within the framework of the EUROfusion Consortium and has received funding from the Euratom research and training programme 2014-2018 under grant agreement No 633053. The views and opinions expressed herein do not necessarily reflect those of the European Commission.

[1] B. Schweer *et al.* *Journal of Nuclear Materials*, **196-198**, 174 (1992).

[2] M. Brix *et al.* *24th EPS Conference, Berchtesgaden, Germany*, **Contrib. Papers Vol 21A, Part IV**, 1837 (1997).

[3] S. Brezinsek *et al.* *Fusion Science and Technology*, **47** (2), 209 (2005).

[4] S. Davies *et al.* *Journal of Nuclear Materials*, **241-243**, 426 (1997).

[5] M. Griener *et al.* *Plasma Physics and Controlled Fusion*, **60** (2), 025008 (2018).

[6] T. Barbui *et al.* *Review of Scientific Instruments*, **87** (11), 11E554 (2016).

[7] E. de la Cal *et al.* *Plasma Physics and Controlled Fusion*, **53** (8), 085006 (2011).

[8] M. Goto *et al.* *Journal of Quantitative Spectroscopy and Radiative Transfer*, **137**, 23 (2014).

[9] S. Kajita *et al.* *Physics of Plasmas*, **13** (1), 013301 (2006).

[10] D. Reiter *et al.* *Plasma Physics and Controlled Fusion*, **33** (13), 1579 (1991).

[11] J. M. M. Burgos *et al.* *Physics of Plasmas*, **19** (1), 012501 (2012).

[12] O. Schmitz *et al.* *Plasma Physics and Controlled Fusion*, **50** (11), 115004 (2008).

[13] M. Goto. *Journal of Quantitative Spectroscopy and Radiative Transfer*, **76** (3–4), 331 (2003).

[14] Y. Ralchenko *et al.* *Atomic Data and Nuclear Data Tables*, **94** (4), 603 (2008).

[15] G. W. F. Drake *et al.* *Physical Review A*, **46** (5), 2378 (1992).

[16] M. Krychowiak *et al.* *Plasma Physics and Controlled Fusion*, **53** (3), 035019 (2011).

[17] D. Nishijima *et al.* *Plasma Physics and Controlled Fusion*, **49** (6), 791 (2007).

[18] S. Kajita *et al.* *Physics of Plasmas*, **16** (6), 063303 (2009).

[19] O. Neubauer *et al.* *Fusion Engineering and Design*, **96**, 891 (2015).

[20] EIRENE. `http://www.eirene.de/`. Last visited on March 6, 2018.

[21] D. Reiter *et al.* *Fusion Science and Technology*, **47** (2), 172 (2005).

[22] W. Zholobenko *et al.* Development and evaluation of a synthetic helium beam diagnostic for Wendelstein 7-X. Technical Report Juel-4407, Forschungszentrum Jülich GmbH (2018). `http://hdl.handle.net/2128/17601`.

[23] M. Brix. *Messung von Elektronentemperatur und -dichte mittels Heliumstrahldiagnostik im Randschicht-plasma eines Tokamaks*. Ph.D. thesis, JÜL-Report 3638, Forschungszentrum Jülich (1999). Revisited in: [12].

[24] D. Reiter *et al.* *Journal of Nuclear Materials*, **196-198**, 1059 (1992).

[25] E. de la Cal *et al.* *Nuclear Fusion*, **48** (9), 095005 (2008).

[26] H. Frerichs *et al.* *Review of Scientific Instruments*, **87** (11), 11D441 (2016).

[27] H. Frerichs *et al.* *Nuclear Fusion*, **57** (12), 126022 (2017).

[28] T. Fujimoto. *Journal of Quantitative Spectroscopy and Radiative Transfer*, **21** (5), 439 (1979).

[29] P. Bachmann *et al.* *Contributions to Plasma Physics*, **35**, 45 (1995).

[30] D. Reiter *et al.* *Plasma Physics and Controlled Fusion*, **44** (8), 1723 (2002).

[31] D. Reiter *et al.* *Journal of Nuclear Materials*, **313-316**, 845 (2003). Plasma-Surface Interactions in Controlled Fusion Devices 15.

[32] J. L. Terry *et al.* *Physics of Plasmas*, **5** (5), 1759 (1998).

[33] C. Maggi *et al.* *Journal of Nuclear Materials*, **266-269**, 867 (1999).

[34] M. Griener *et al.* *Review of Scientific Instruments*, **88** (3), 033509 (2017).

[35] Y. Feng *et al.* *Journal of Nuclear Materials*, **266-269**, 812 (1999).

[36] M. Rack *et al.* *Nuclear Fusion*, **57** (5), 056011 (2017).

[37] HYDKIN online solver. `http://www.hydkin.de/cgi-bin/eigen.cgi?datenart=he&timest=1&neu=neu&submit=ENTER+online+solver`. Last visited on June 2, 2018.

[38] I. Bray. *Phys. Rev. A*, **49**, 1066 (1994).

[39] Y. Ralchenko. Private communication (2017).

[40] D. V. Fursa *et al.* *Journal of Physics B: Atomic, Molecular and Optical Physics*, **30** (4), 757 (1997).

[41] K. Bartschat. *Journal of Physics B: Atomic, Molecular and Optical Physics*, **31** (10), L469 (1998).

[42] M. Génévriez *et al.* *Phys. Rev. A*, **96**, 010701 (2017).

[43] HYDKIN He database. `http://www.hydkin.de/plotform/index_he.html`. Last visited on June 2, 2018.

[44] I. I. Sobel'man *et al.* *Excitation of Atoms and Broadening of Spectral Lines (Springer Series on Atomic, Optical, and Plasma Physics)*. Springer (2002). ISBN 978-3-540-58686-9.

[45] H. R. Griem. *Physical Review*, **128** (3), 997 (1962).

[46] J. A. Kunc *et al.* *The Astrophysical Journal*, **396**, 364 (1992).

[47] D. Salzmann. *Atomic Physics in Hot Plasmas*. OXFORD UNIV PR (1998). ISBN 0195109309.

[48] Jülich Supercomputing Centre. *Journal of large-scale research facilities*, **2** (A62) (2016).